Structural characterization and *in-vivo* reliability evaluation of silicon microneedles

Conor O'Mahony

Abstract This work presents an analysis of the failure mechanisms, structural properties and reliability of wet-etched silicon microneedles, which have wide-ranging applications in transdermal delivery, sensing and diagnostics. For the first time, *in-vivo* skin insertion forces are measured and the structural properties of individual silicon microneedles are assessed using both compression and shear tests. Compressive failure of this particular microneedle design does not occur because of buckling, but instead is predominantly due to progressive fracture along the relatively weak {111} crystal plane. Compressive and shear failure strengths are experimentally determined to be (2.9 +/− 0.3) GPa and (9.2 +/− 0.2) MPa, respectively. It is also shown that basic mechanical tests that are commonly used in the field of microneedle development may significantly underestimate safety factors for this type of needle due to the unrepresentative nature of the interaction of a rigid surface with the needle tips. Therefore, a new figure-of-merit for the reliability of such microneedles is proposed, which is based on the ratio of material failure strength to peak stress during skin insertion. The distribution of forces over the sharp, conical needle tip during skin penetration leads to a very large safety margin of over 700, and a correspondingly high degree of reliability when applied to *in-vivo* human tissue.

C. O'Mahony (✉)
Tyndall National Institute, University College Cork, Cork, Ireland
e-mail: conor.omahony@tyndall.ie

1 Introduction

The outer layer of human skin, the stratum corneum (SC), is composed of dead, keratin-filled cells embedded in lipid bilayers and moisture. This 10–20 μm thick layer prevents water loss from the body and also acts as a barrier against external contaminants and environmental influences. Lying beneath the stratum corneum are the two other primary skin layers; namely the viable epidermis, a 50–100 μm thick layer devoid of blood vessels but rich in immunologically-active cells such as Langerhan's cells, and the dermis, a 1–3 mm thick layer of supporting tissue containing nerve endings, blood vessels, hair follicles and sweat glands (Tobin 2006).

The SC acts as a major impediment to the transdermal delivery of therapeutic agents, meaning that drug delivery via the skin is currently limited to a small number of low dose (~10 mg/day), low molecular weight (<500 Da), high lipophilicity drugs such as nicotine for smoking cessation, nitroglycerin for cardiac conditions, scopolamine for motion sickness, testosterone for hormone replacement therapy, and fentanyl for pain management (Tanner and Marks 2008). The SC layer also has a remarkably high resistance to the flow of electrical current. Many diagnostic procedures and therapies such as physiological signal monitoring or electroporation (Webster 2010) rely on external skin electrodes for the transfer of electrical signals or stimuli either to or from the body, and the high impedance of the stratum corneum greatly reduces the efficacy of such procedures.

In recent years there has been considerable interest in the development of microneedle technologies to overcome the stratum corneum barrier in a minimally invasive manner (Pettis and Harvey 2012; van der Maaden et al. 2012; Kim

et al. 2012; Broderick 2012). Fuelled by recent advances in micromachining and materials processing, these sharp-tipped, micron-scale projections are generally less than 1 mm in length, and are made using a variety of fabrication processes in very diverse materials (Donnelly et al. 2010). Microneedles are available in either solid or hollow forms. Solid microneedles create transient micropores or perforations in the skin's stratum corneum, thereby increasing the permeability of the barrier layer to large molecules by several orders of magnitude; medicants can be incorporated in dissolvable needles, included in microneedle coating formulations, or simply topically applied to the skin before or after microneedle application. Hollow microneedles incorporate a narrow bore or capillary through which therapeutic agents can be injected directly into the lower skin layers (van der Maaden et al. 2012). So-called 'dry electrodes' for physiological signal monitoring use an array of sharp microneedles to penetrate the resistive SC and contact the conductive underlying skin layers, thereby bypassing the SC barrier layer and removing the need for painful skin abrasion and messy gel application (O'Mahony et al. 2012).

Since microneedle heights can be chosen so as to penetrate the stratum corneum whilst avoiding stimulation of the underlying nerve endings that lie deeper in the epidermis, the minimally-invasive and painless nature of microneedle application make this a very attractive technology (Haq et al. 2009). Other advantages include avoidance of the first-pass metabolic effect in the liver, controllable dose delivery, high patient compliance, dose sparing, elimination of needle-stick injuries, and removal of the need for a trained healthcare practitioner (Birchall et al. 2011). To date, a number of groups have investigated the applicability of our wet-etched silicon microneedle technology to drug delivery (O'Brien et al. 2009; Bedoni et al. 2009; Abla et al. 2013), vaccine delivery (Vrdoljak et al. 2012; McGrath et al. 2011; Carey et al. 2011), pDNA delivery (Pearton et al. 2008; Coulman et al. 2006), photodynamic therapy (Donnelly et al. 2008, 2009), electroporation (Wilke et al. 2005a) and physiological signal monitoring (O'Mahony et al. 2012; Pini et al. 2012). This paper assesses the structural robustness and reliability of these silicon microneedles, measures *in-vivo* skin penetration forces and presents a new figure-of-merit for the biomechanical reliability of such structures.

1.1 Microneedle array design and reliability

Microneedle-based devices must be sharp and slender enough to easily penetrate skin, yet strong enough to ensure that needles do not fracture and lodge in the skin. Two primary biomechanical parameters apply to the safe and efficient design of microneedles: these are (a) the force at which the structural integrity of the microneedle fails and (b) the force required to insert the microneedle into skin. The ratio of these two forces is commonly termed the 'safety factor' or 'safety margin' (Davis et al. 2004) and microneedle designers aspire to have this ratio as high as possible in order to allow for variations in user application methods, skin thickness, etc.

The insertion force may be measured in a number of ways including dye marking (Li et al. 2010), force-displacement tests (Davis et al. 2004) or electrical measurements (Roxhed et al. 2007). Failure forces are usually evaluated by pressing devices into a rigid surface, and microneedles are assumed to fail during insertion due to compression or buckling along their central axis, or bending and shearing due to forces acting in the lateral direction (Davis et al. 2004; Aggarwal and Johnston 2004).

Although a large body of work has published on the subject of microneedle mechanics, little has been written specifically on the structural characterisation of out-of-plane silicon microneedles. It has known for some time that arrays of dry-etched, columnar silicon microneedles can be inserted into *ex-vivo* human skin with only minor failure in a few per cent of needles (Henry et al. 1998). In (Ji et al. 2006), analytical models for the critical compressive loading of porous, pyramidal silicon microneedles were developed, while preliminary mechanical analyses of arrays of our wet-etched silicon microneedles have also been presented (Forvi et al. 2012; Wilke et al. 2005a, b).

These wet-etched needles are shaped in the form of an octagonal cone, with sidewall angles of 71.6° and tip radii as low as 50 nm. In this paper, for the first time, *in-vivo* skin insertion forces are measured and the structural properties of individual silicon microneedles are assessed using both compression and shear tests. In contrast to other types of microneedle, which are often columnar in nature and usually composed of amorphous materials, this paper shows that compressive failure of this particular microneedle design does not occur because of buckling, but instead is predominantly due to progressive fracture along the relatively weak {111} crystal plane.

Results from standard mechanical characterization procedures are compared with those obtained from reliability tests in *in-vivo* human skin to demonstrate that such basic mechanical tests may significantly underestimate safety factors for this type of needle due to the unrepresentative nature of the interaction of a rigid surface with the sharp microneedle tips. Finally, it is shown that the distribution of forces over the needle tip and conical structure during skin penetration leads to a very high degree of microneedle reliability, and a correspondingly large safety margin. A new figure of merit for needle reliability, based on the ratio of material failure strength to peak stress experienced during skin insertion, is proposed to reflect this.

2 Microneedle fabrication

The microneedle arrays were fabricated using potassium hydroxide (KOH) wet-etching techniques, an etch mechanism

that has been extensively described in (Wilke et al. 2006; Wilke and Morrissey 2007). Briefly, the starting material is a boron doped, 100 mm diameter monocrystalline silicon wafer (Silicon Valley Microelectronics, Santa Clara, CA), orientated in the <100> direction and onto which square oxide/nitride masks have been patterned using standard photolithography tools. These masks are aligned with the <110> direction and the height of the subsequent microneedle is a linear function of the mask square side length.

The patterned silicon wafer is then etched in a 29 % w/v aqueous KOH solution until convex corner mask undercut takes place, the eight planes intersect and a needle shape is formed, Fig. 1. This needle is comprised of eight {263} planes, a base of {212} planes and has a height:base diameter aspect ratio of 3:2. Tip sharpness is a function of mask and crystal axis alignment accuracy; tip radii are generally of the order of 50–100 nm.

3 Experimental

3.1 Application of compressive forces

By asking volunteers to apply thumb pressure to a force gauge, it has been determined that the maximum force typically used to apply a 1 cm^2 microneedle array to a human subject is in the region of 30 N. Since our designs feature 10–100 microneedles per array, a microneedle could therefore be subjected to maximum compressive forces of approximately 3 N during normal application by hand.

With this limit in mind, microneedle failure under compressive forces was assessed using a computer-controlled force-displacement station (Model 5565, Instron,
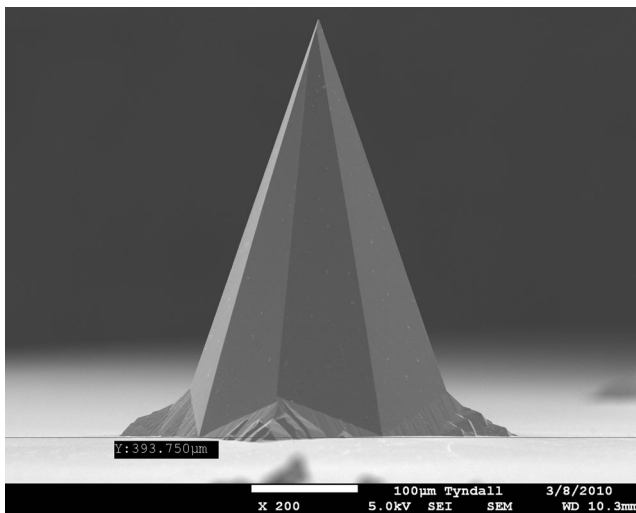

Fig. 1 Solid silicon microneedle. The design height of this needle is 400 μm

Buckinghamshire, UK). A custom-machined, 5 mm diameter aluminium rod was mounted on the load cell of the instrument and was pressed against a single 300 μm tall microneedle at a rate of 1 μm/s until the desired maximum load of 3 N was reached. The force-displacement station recorded time, array displacement and the force applied to the array with resolutions of 2 ms, 1 μm and 1 mN, respectively.

3.2 Application of shear forces

Measurements of microneedle shear strength were carried out using a Royce 552 bond test system (Royce Instruments, Napa CA)—a tool used for carrying out measurements of wirebond strength and reliability in the microelectronics industry. The system incorporates a shear test fixture, which was positioned at varying distances below the tip of a microneedle and moved at a speed of 25 μm s^{-1} in the lateral direction until contact with the needle was made and shear occurred. Needles were sheared at distances of between 20 μm and 160 μm from the tip, and 20 samples were measured at each shear height.

3.3 *In-vivo* skin insertion force measurement

Microneedle insertion tests were performed on a healthy 36-year-old Caucasian male, from whom informed consent was obtained prior to the study. The protocol was approved by the Clinical Research Ethics Committee of the Cork Teaching Hospitals.

The subject was seated at a computer-controlled test station as described above. Tests were carried out at locations on both the volar and dorsal forearm; in both cases, the subject's skin was lightly shaved using a disposable safety razor 24 h prior to the test. No other skin preparation or modification was carried out. Microneedle arrays were first sterilised by immersion in 70 % ethanol for 30 min. The arrays were affixed to a custom-machined, 5 mm diameter aluminium rod using double-sided adhesive tape (3 M, Austin, Tx); this rod was then mounted on the load cell of the instrument.

Tests were performed by placing the subject's arm horizontally beneath the force-displacement tool and keeping the arm immobile during the procedure. The microneedle array was pressed against the subject's arm at a rate of 1 mm/s until the desired maximum load was reached.

In order to visually assess microneedle penetration efficacy, approximately 200 μl of 2 % w/v methylene blue dye was applied to the test site immediately after removal of the array and left for 5 min before excess dye was removed using a vigorous scrubbing action under cold running water. The site was then examined using a stereozoom microscope (SZX12, Olympus Inc., Center Valley, PA, USA).

3.4 *In-vivo* reliability

Numerous controlled insertion force studies, such as those outlined in Section 3.3, have shown no evidence of structural failure of the microneedles used. Additionally, to more realistically mimic 'real-world' use, arrays of 36 microneedles arranged in a 6×6 configuration on a 7 mm×7 mm die were first autoclave sterilised and then affixed to the central fabric region of a self-adhesive wound dressing (Elastoplast 48599, Beiersdorf AG, Germany) using a 12 mm×12 mm×1.2 mm-thick pad of double-sided adhesive tape (686–1154, Radionics, Ireland) as shown in Fig. 2. The ventral forearm of a 37-year old Caucasian volunteer was cleaned using an ethyl alcohol antimicrobial skin wipe (Purell, GOJO Industries, Inc., OH, USA) and the assembly was applied to the arm using moderate finger pressure (it was estimated that maximum applied forces were in the region of 8–12 N) and a lateral rubbing motion to mimic typical transdermal patch application, before being left in place for 6 h while the volunteer carried out normal daily (office-based) activities. The procedure was repeated ten times, using a new microneedle array each time. Both before application and after removal, each individual microneedle was inspected from three different directions using an optical microscope (SZX12, Olympus Microscopy, UK) at a magnification of 90X; representative samples were also examined using scanning electron microscopy (SEM) (FEI, OR, USA). A control device, consisting of a flat 7 mm×7 mm silicon die, was assembled and applied in a similar manner.

4 Results and analysis

4.1 Compressive loading - results

Microneedle reliability under compressive loading is generally assessed by inspecting a force-displacement curve, where a sharp discontinuity in the curve is taken as an indication of structural failure of the needle, usually due to buckling (Davis
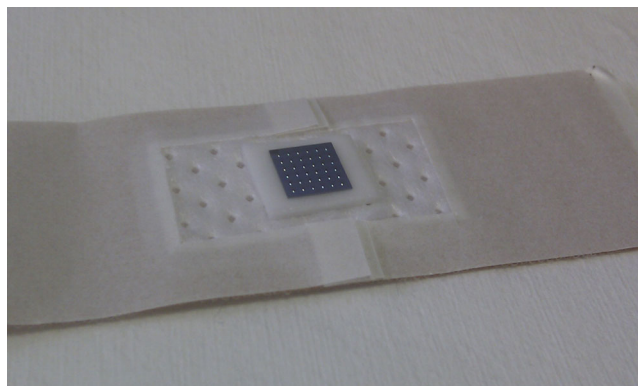

Fig. 2 Wearable patch prototype for reliability assessment of needles

et al. 2004; Paik et al. 2004; Park et al. 2005; Khanna et al. 2010). For this work, over 50 force-displacement tests were carried out on individual 300 μm tall needles at maximum applied forces ranging from 0.1 N to 3 N. Representative results are shown in Fig. 3, below. Fracture discontinuities are rarely apparent and the forces at which these discontinuities occur are randomly distributed. In contrast to other works, in a very large majority of cases no discontinuities characteristic of microneedle failure have been observed, even at forces as high as 25 N/needle (data not shown).

4.2 Compressive loading - modelling and analysis

It is generally assumed that microneedles subjected to a compressive force fail due to buckling or fracture (Henry et al. 1998; Aggarwal and Johnston 2004). It has been shown (Smith 1988) that the critical buckling force, P_{cr}, of a tapered polygonal column of height h can be evaluated by solving the equation

$$P_{cr} = \frac{\pi^2 E}{2h^3} \int_0^h I(z)\cos^2\left(\frac{\pi z}{2h}\right)dz, \tag{1}$$

where E is the Young's modulus of the material and $I(z)$ is the area moment of inertia which may be defined as $I(z)= 0.0547d^4$ for an octagonal cone of diameter d, where $d=2z/\arctan(3)$ and z is the distance from the apex of the cone. This expression has been solved using Matlab for the needle geometry defined in Section 2 and is shown in Fig. 4.

Clearly, these predicted failure forces (in the region of 12 N for a 300 μm tall microneedle) do not correspond to experimental observations, and therefore it is clear that buckling is not the dominant failure mechanism.

All microneedles were subsequently imaged using scanning electron microscopy. Although it has already been shown that in most cases no force-displacement discontinuities characteristic of structural failure were observed (Fig. 3), varying degrees of damage are visible on every needle, Fig. 5. The damage has been characterised by measuring the size of the broken particle l_c, which is defined as the length from the apex of the microneedle to the intersection of the longitudinal axis of the microneedle and the broken plane.

A closer inspection of the microneedles reveals that the damaged needle tips show a characteristic sloped shape, indicating that failure takes place along the relatively weak {111} plane, which has an angle of 54.7° to the horizontal, and which is a preferred cleavage plane in single-crystal silicon (Miller et al. 2007). The lack of regular, sharp discontinuities in the curves of Fig. 5 also indicates that failure generally takes place through a gradual 'grinding' mechanism of these planes, rather than a sudden, catastrophic failure of the structure.
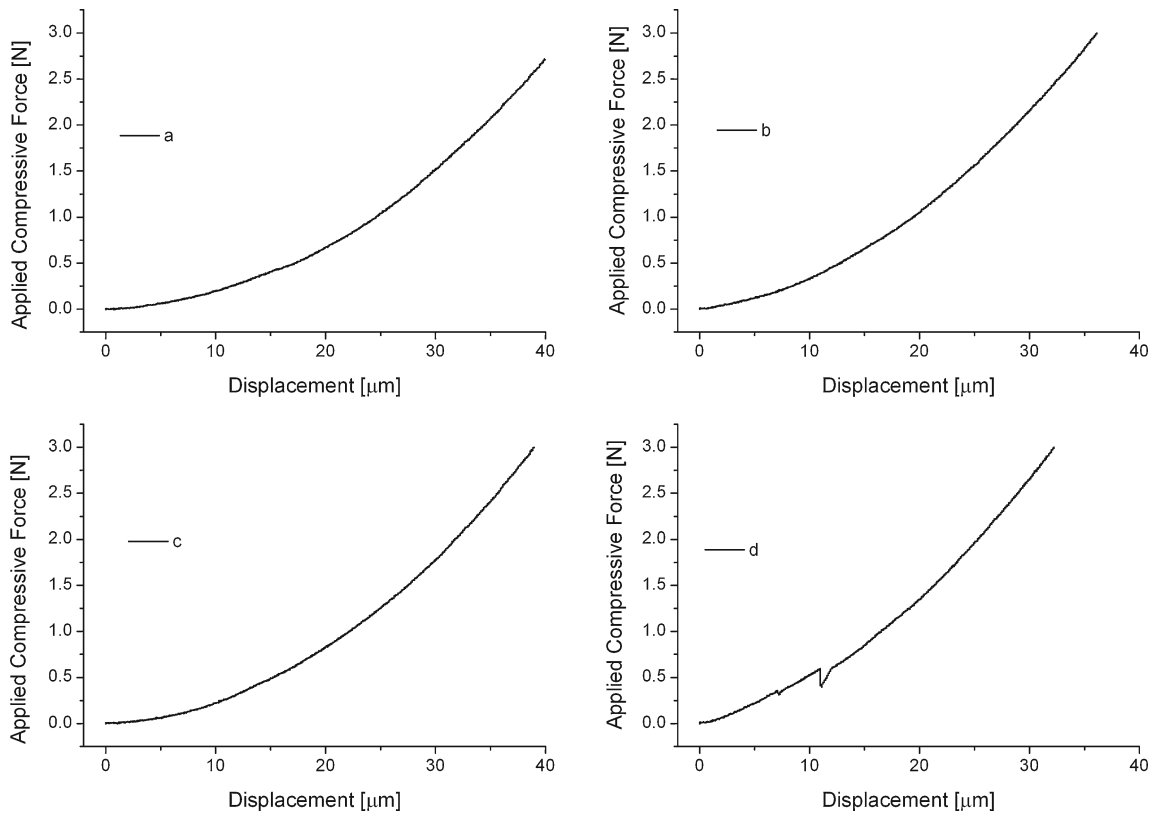
Fig. 3 Representative examples of force-displacement tests

Therefore, these microneedles do not fail due to buckling, but instead fail due to the presence of a shearing component of the compressive force along this weak {111} plane. The vertical compressive force, F, exerted on the microneedle may be resolved into two vector components—one acting normal to, and the other parallel to, the {111} plane, Fig. 6(a). The magnitude of the parallel shearing component is given by $F_s = F\sin(54.7°)$, Fig. 8(a). This shear force will result in failure of the needle at a point where the cross-sectional area of the fractured {111} plane, A, is defined as $A = F_s/G$, where G is the failure strength of the material.

Fig. 4 Predicted buckling forces as a function of microneedle height

In order to model the height of the broken tip l_c as a function of applied force F, it is assumed that the shear area created by the intersection of the {111} plane with the octagonal microneedle forms an ellipse that is characterised by minor axis a, major axis b and has an area equal to $\pi ab/4$ as illustrated in Fig. 6(b).

Using trigonometric relations, the angle of the needle sidewalls, and the angle of the sheared {111} plane (54.7°), it may be calculated that

$$b = 1.484l_c; \tag{2}$$

$$a = \cos(54.74)b = 0.856l_c; \tag{3}$$

$$A = 0.997l_c^2; \tag{4}$$

$$l_c = \sqrt{\frac{0.818F}{G}}. \tag{5}$$

This dependence of shear particle size on compressive force has been experimentally measured and is shown in Fig. 7.

The data has been fitted to Eq. (5) using $G = (2.9 +/- 0.3)$ GPa, which is in agreement with the values of 0.3 GPa–7.2 GPa reported for the shear strength of single-crystal silicon
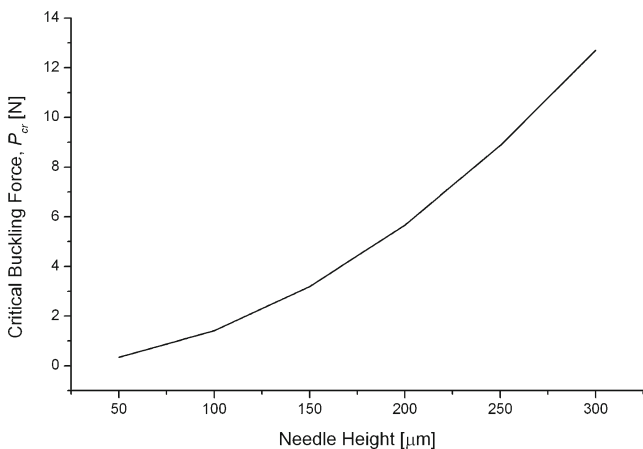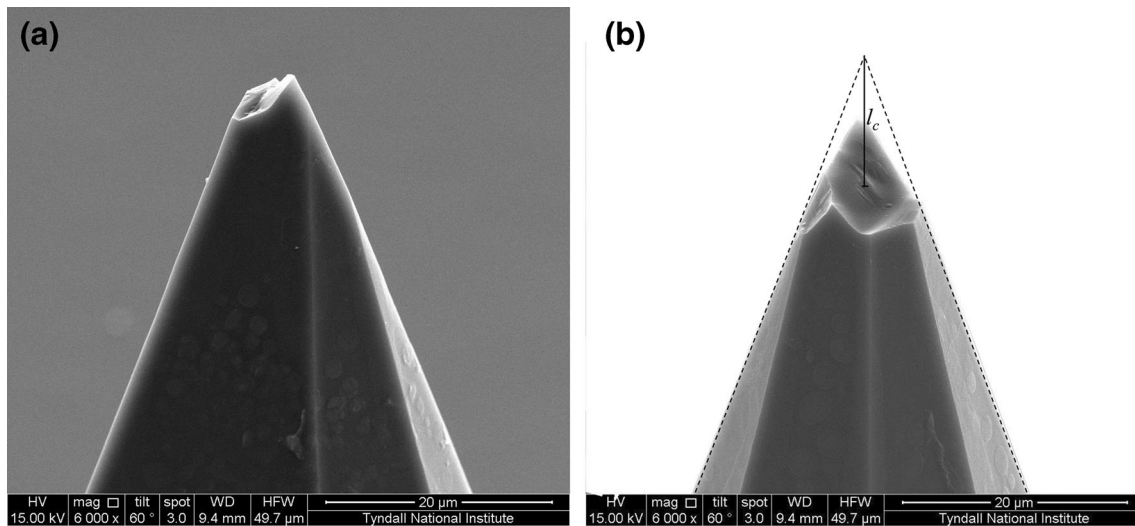
Fig. 5 Examples of damage to needle after application of 0.3 N and 0.5 N compressive loads to the needle tip. **b** also defines the size of the broken particle l_c as the distance from the needle apex to the intersection of the longitudinal axis of the microneedle and the broken plane. In this case, l_c is 14 μm

in works summarised in (Miller et al. 2007). This simple model provides a useful estimate of the degree of damage likely to occur when a rigid surface is applied to the needle tip using a compressive force. It does, however, become inaccurate at low forces, where the surface-to-volume ratio of the sheared particle becomes large and surface defects, tip misalignment artefacts and the presence of rapidly converging plane edges provide an increased probability of locations where crack initiation can take place.

4.3 Shear loading - results and analysis

Inspection of sheared microneedles using scanning electron microscopy reveals that needles subjected to lateral forces also fail along the {111} plane, Fig. 8.

This interaction is modelled by assuming that a lateral force F acting on the needle at a distance l_s from the tip results in a shearing force component F_s, and that the resulting sheared area created by the intersection of the {111} plane with the octagonal microneedle is approximated to an ellipse (Fig. 9).

In a similar manner to the analysis in Section 4.2 and (Wilke et al. 2005b), it may be shown that

$$F = 3.965 G_s l_s^2 \qquad (6)$$

This relationship has been fitted to a plot of F against l_s with shear strength $G_s = (9.2 +/- 0.2)$ MPa, Fig. 10. The shear forces observed are in broad agreement with those in the range of 0.35–2.7 N observed for larger, hollow silicon needles (Khanna et al. 2010), for a smaller subset of needles identical
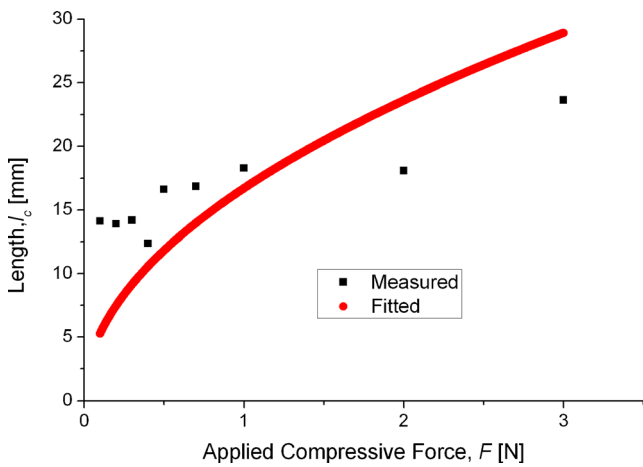
Fig. 6 Compressive force model
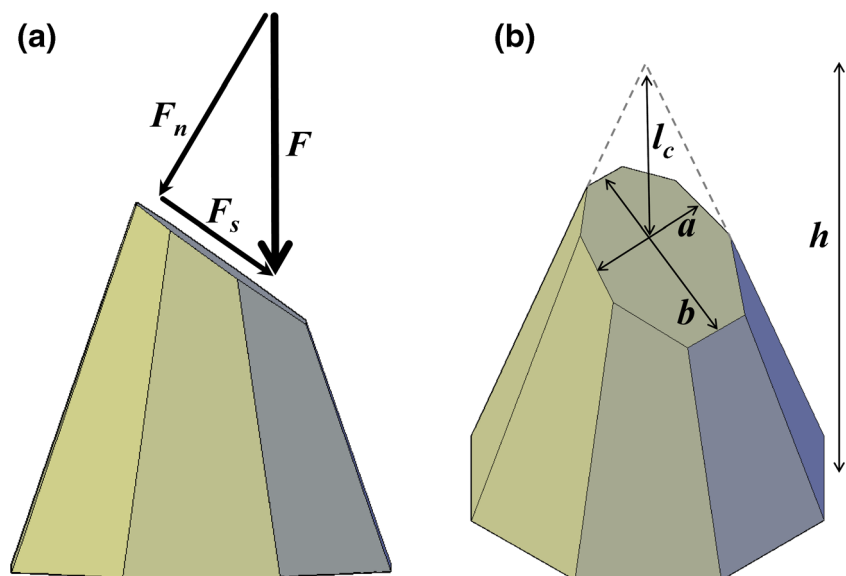
Fig. 7 Measured and analytically estimated shear particle sizes as a result of compressive loading

Fig. 9 Shear force model

to these (Wilke et al. 2005b), and for silicon microridges (Chen et al. 2000).

4.4 *In-vivo* skin insertion forces

Methylene blue dye is used as a skin staining agent and has previously been used to indicate the site of microneedle penetration (Li et al. 2010). In this study, staining clearly indicated the presence of conduits formed as a result of microneedle insertion, Fig. 11. For each test site, the number of conduits formed was recorded as a function of maximum application force per needle, and results are shown in Fig. 12 (averaged over four test sites).

Over 95 % penetration is observed for forces of greater than 15 mN per needle (1.2 N per array). These figures are in close agreement with other work on ultrasharp microneedles (Roxhed et al. 2007). Confirmation of 100 % penetration has never been achieved; this is because at least one of the 81 needles on the array usually falls close to or on a hair follicle and this prevents conclusive identification of an insertion mark at that point.
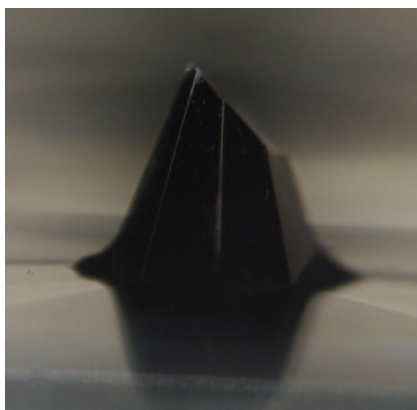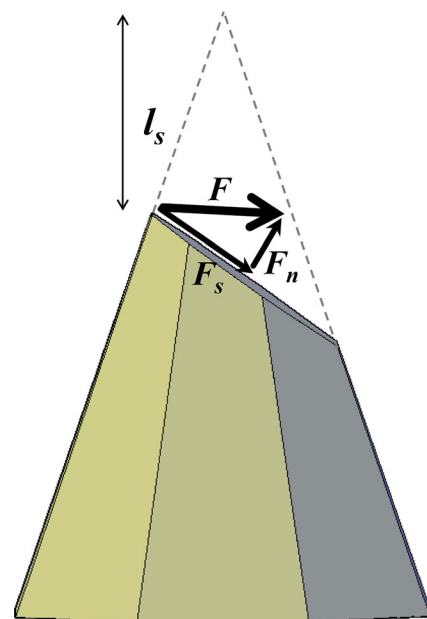
4.5 *In-vivo* microneedle reliability

No pain was reported during application of the patch prototype, although a slight stinging sensation was reported in three of the ten cases. Following removal, a mild and well-defined, but transient, erythema in the shape of the 7 mm×7 mm silicon die was observed at the site of all ten patches. This was barely perceptible after 6 h and had disappeared entirely after 12 h. No bleeding or blood spots were observed at any time. A much milder erythema, concentrated around the edges of the die, was observed after removal of the control device. This faded rapidly and had completely disappeared after 2 h.

Both before and after the procedure detailed in Section 3.4, every microneedle (i.e. a total of 360 needles on ten arrays)
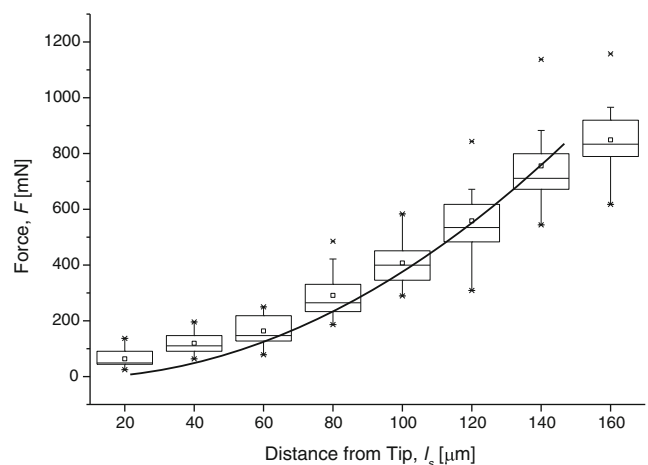

Fig. 8 Sheared, 700 μm tall microneedle, illustrating failure along the sloped {111} plane

Fig. 10 Microneedle shear measurement and forces. The solid line is Eq. 6 fitted to the mean values of shear force measurements ($n=20$ needles) with $G_s=9.2$ MPa
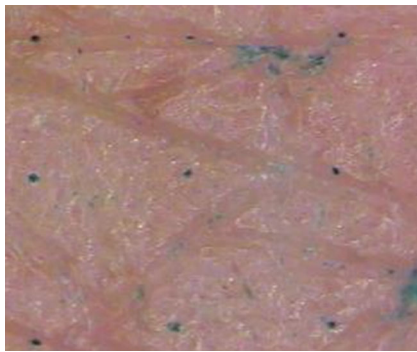
Fig. 11 Methylene *blue-stained in-vivo* human skin after array application at 20 mN per needle. Conduits formed after needle insertion and staining are clearly visible as *dark blue dots*; the spacing between insertion sites is 1 mm

was individually inspected using an optical microscope (SZX12, Olympus Microscopy, UK) at a magnification of 90X. No fracture or failure of any needle was observed. A representative sample was also examined using scanning electron microscopy as shown in Fig. 13, which also illustrates that the tip is undamaged even after skin insertion and wear and has a radius of approximately 60 nm.

5 Discussion

Insertion forces for these needles are comparable to the lowest reported in the field (Roxhed et al. 2007); over 90 % of the needles on 81-needle arrays penetrate skin at forces of 15 mN per needle. These very low forces increase needle reliability and also allow array designers to increase the number of needles on an array, thereby leading to increased skin permeability and device efficacy.

The mechanical tests described earlier, and commonly used in structural analyses of microneedles, show that these wet-
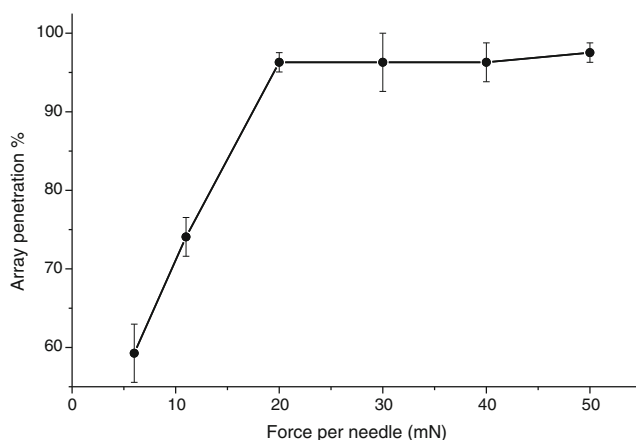

Fig. 12 Array penetration percentage as a function of applied force per needle. There are 81 microneedles per array

etched silicon needles subjected to compressive stress fail due to continuous shearing along the relatively weak {111} plane, and that some damage occurs even at very low forces due to the sharp nature of the needle tips. However, it is also clear that all of our *in-vivo* (both human and animal) experience shows that these conical needles are extremely reliable and that failure is very rare when properly applied to tissue.

The discrepancy is due to the extremely high stresses generated when nanometer-scale microneedle tips are pressed against a rigid surface, which easily exceed material fracture strengths. In reality, this type of simple rigid-body interaction does not occur when microneedles are used in practice, and so is an unreliable method of assessing structural reliability. Instead, compliant skin tends to conform to the shape of the tip before, during and after insertion (Martanto et al. 2006; Roxhed et al. 2007; Enfield et al. 2010). A simple model is now proposed, based on the assumptions that tissue conforms perfectly to the needle shape during the insertion process, and that the needle-skin interfacial area, A_I, is equal to the octagonal cross-sectional area of the needle. This can be defined as a function of array displacement after initial skin contact s as

$$A_I = 2.828 \left[\frac{s}{3} \right]^2 ; s < h \qquad (7)$$

$$A_I = A_b ; s \geq h, \qquad (8)$$

where A_b is the area of the array baseplate associated with each needle, and is equal to 1 mm^2 for this case. Note that for this particular shape, A_I increases rapidly as the needles are inserted into the skin, Fig. 14.

To experimentally assess the practical effects of this interaction, an array of 300 μm tall needles was pressed into the forearm of a human subject using the controlled force-displacement setup described in Section 3.4. The resultant stress acting on each needle was calculated as $\sigma(s)=F(s)/A_I$, where $F(s)$ is the experimentally measured force-displacement relationship. This is graphically illustrated in Fig. 15, where the sharp drop in stress at $s=300$ μm represents the contact of the base of the microneedle array with the skin surface, i.e. $s = h$. Note that this occurs even before penetration takes place, significantly relieving stress on the needle itself at an early stage.

Even this rather basic model, which neglects complex skin deformations and puncture mechanics, explains the high degree of reliability observed when using these needles. Firstly, the maximum compressive stress (<10 MPa) experienced during insertion is much less than that required to cause significant shear failure along the {111} plane. Secondly, due to the conical shape of the needles, this stress actually decreases rapidly during the initial stages of needle-skin engagement, further reducing the likelihood of failure. Once $s = h$, the stress decreases sharply still further as the base of the
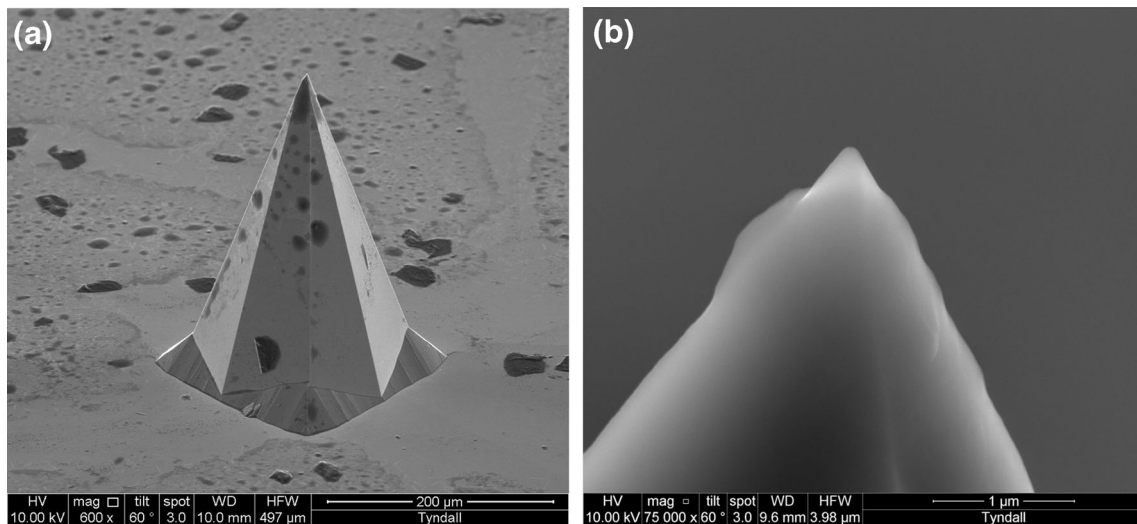
Fig. 13 **a** 300 μm tall microneedle after the six-hour wear period as described in Section 4.5. Skin and cellular debris is visible on and around the needles but structural integrity remains fully intact. **b** Closeup of the tip of the same needle, which is visible poking through a layer of skin debris. The tip is undamaged and has a radius of approximately 60 nm

needle comes into contact with the skin, and is now several orders of magnitude below that needed to cause failure. The final phase of the plot shows an approximately linear increase in stress as elastic deformation of the skin occurs, although stress values are still well below failure strengths.

Since it is therefore apparent that current estimations of microneedle safety margins often rely on structural tests involving rigid surfaces and do not accurately reflect realistic usage conditions, a new figure of merit for microneedle reliability is proposed that is based on measured microneedle-skin interactions. Assuming that the risk of shear failure is negligible for a correctly applied array, the safety margin of the needle, S_n, is defined as the ratio of the failure strength of the microneedle as evaluated in Section 4.2 to the peak compressive stress experienced during application as measured in Fig. 15, i.e.

$$S_n = \frac{G}{\sigma_{\max}}. \qquad (9)$$

In this case, peak stress is experienced during first contact with the skin and is approximately 4 MPa. As estimated in

Fig. 7, the failure strength of the needle is 2.9 GPa, giving a safety margin of over 700. This is substantially higher than the safety margins reported for most designs, which are in the region of 1–20 (Davis et al. 2004; Khanna et al. 2010; Sullivan et al. 2010).

The second failure mode considered in this work is that of shear failure, and an analysis of lateral forces acting on single microneedles reveals that needle tip sections of ~50 μm will shear off at relatively low forces of 0.1 N per needle. It is important to note that these lateral forces will arise only when arrays are misused through scraping along the skin or insertion in an inappropriate manner, and will furthermore be distributed among all needles on the array, thereby reducing the likelihood of failure. Secondly, should failure occur, the elastic nature of the skin and the force exerted by the skin on the sloped sidewalls of the needle results in an upward component of force that will push these conical particles upwards and out
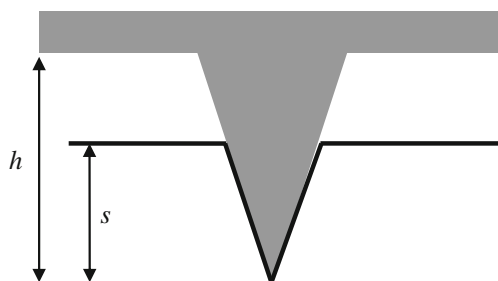

Fig. 14 Simple model of microneedle insertion into skin. Note that for this geometry the interfacial area increases rapidly with insertion depth
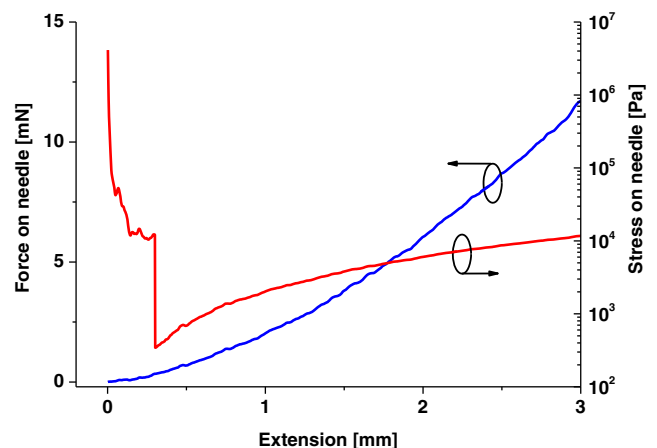

Fig. 15 Measured insertion forces and stress acting on the microneedle as a function of needle displacement

of the skin. In addition, the epidermal skin layers are renewed in such a manner that the outer skin cells are pushed upwards and shed from the body every 2–3 weeks (Cowen et al. 2001), which assists in ejecting foreign particles from the skin. Finally, the shear issue may well be irrelevant as microneedle arrays are likely to be used using applicator devices (Singh et al. 2011), which apply needles in a direction that is normal to the skin surface and which will eliminate shear forces that arise from incorrect application.

6 Conclusion

This paper has analysed the failure mechanisms and *in-vivo* reliability of wet-etched, ultrasharp silicon microneedles. It has been shown that the primary failure mode of these microneedles is by brittle fracture along the relatively weak {111} silicon plane, whether compressive or lateral forces are applied. No single point of failure is identified under compressive forces, and instead experiments show that the degree of failure is a continuous function of applied force.

Microneedles are commonly characterised by pressing the structure against a rigid surface such that a load is applied to the vertical axis of the needle. Although such compressive tests are reasonably accurate for needles with relatively flat or blunt tips and/or constant columnar cross-sectional area, they are inappropriate for characterisation of needles of this type, where the very low interfacial area of the ultrasharp tips mean that extremely high pressures are exerted on the tips and the brittle nature of silicon means that corresponding fractures are easily attained during the test procedure.

In response to these limitations, this paper has developed a new model that takes into account the fact that tissue tends to conform to the shape of the microneedle tip, and that the conical nature of these structures causes the microneedle-skin interfacial area to increase as skin insertion takes place. Both conditions lead to a rapid decrease in compressive stress acting on the needle-skin interfacial area as the microneedle penetrates into the skin, and in addition this stress suddenly and significantly drops further as the base of the array contacts the skin. Hence, the possibility of microneedle failure actually decreases as skin insertion progresses. This means that reliability of these microneedles, when used in practical applications, is significantly higher than predicted using standard compression tests. In fact, repeated insertion and wear tests using human subjects has failed to result in damage to microneedles arrays, and this agrees with our experience when using silicon microneedles for a wide range of *in-vivo* tests over a significant timespan.

Based on this model, a new and more realistic figure-of-merit for the reliability of such microneedles has also been proposed, which utilizes the ratio of material failure strength to peak stress during skin insertion. The distribution of forces over the needle tip during skin penetration leads to a very large safety margin of over 700, and a correspondingly high degree of reliability when applied to *in-vivo* human tissue.

The results confirm the safety and reliability of silicon microneedles for use in biomedical applications.

References

M. Abla, A. Chaturvedula, C. O'Mahony, A.K. Banga, Ther. Deliv. **4**, 5 (2013)

P. Aggarwal, C.R. Johnston, Sensors Actuators B Chem. **102**, 2 (2004)

M. Bedoni, M. Casella, E. Donetti, E. Forvi, C. O'Mahony, F. Gramatica, Ital. J. Anat. Embryol. **114**, 1 (2009)

J.C. Birchall, R. Clemo, A. Anstey, D.N. John, Pharm. Res. **28**, 1 (2011)

K.E. Broderick, Ther. Deliv. **3**, 8 (2012)

J.B. Carey, F.E. Pearson, A. Vrdoljak, A.M. Crean, P.T. Walsh, C. O'Mahony, A.V.S. Hill, A.C. Moore, PLoS ONE **6**, 7 (2011)

Q. Chen, D.-J. Yao, C.-J. Kim, G.P. Carman, J. Mater. Sci. **35**, 21 (2000)

S.A. Coulman, D. Barrow, A. Anstey, C. Gateley, A. Morrissey, N. Wilke, C. Allender, K. Brain, J.C. Birchall, Curr. Drug Deliv. **3**, 1 (2006)

J.A. Cowen, R.E. Imhof, P. Xiao, Anal. Sci. **17** (2001)

S.P. Davis, B.J. Landis, Z.H. Adams, M.G. Allen, M.R. Prausnitz, J. Biomech. **37**, 8 (2004)

R.F. Donnelly, D.I.J. Morrow, P.A. McCarron, D.A. Woolfson, A. Morrissey, P. Juzenas, A. Juzeniene, V. Iani, H.O. McCarthy, J. Moan, J. Control. Release **129**, 3 (2008)

R.F. Donnelly, D.I.J. Morrow, P.A. McCarron, D.A. Woolfson, A. Morrissey, P. Juzenas, A. Juzeniene, V. Iani, H.O. McCarthy, J. Moan, Photochem. Photobiol. **85**, 1 (2009)

R.F. Donnelly, T.R. Raj Singh, A.D. Woolfson, Drug Deliv. **17**, 4 (2010)

J. Enfield, M.-L. O'Connell, K. Lawlor, E. Jonathan, C. O'Mahony, M. Leahy, J. Biomed. Opt. **15**, 4 (2010)

E. Forvi, M. Bedoni, R. Carabalona, G. Cassarà, P. Mazzoleni, C. Morasso, C. O'Mahony, F. Rizzo, M. Soncini, F. Gramatica, Sensors Actuators A Phys. **180**, 177 (2012)

M.I. Haq, E. Smith, D.N. John, M. Kalavala, C. Edwards, A. Anstey, A. Morrissey, J.C. Birchall, Biomed. Microdevices **11**, 1 (2009)

S. Henry, D. McAllister, M.G. Allen, M.R. Prausnitz, J. Pharm. Sci. **87**, 8 (1998)

J. Ji, F.E.H. Tay, J. Miao, C. Iliescu, J. Micromech. Microeng. **16**, 5 (2006)

P. Khanna, K. Luongo, J.A. Strom, S. Bhansali, Microsyst. Technol. **16**, 6 (2010)

Y.C. Kim, J.H. Park, M.R. Prausnitz, Adv. Drug Deliv. Rev. **64**, 14 (2012)

W.-Z. Li, M.-R. Huo, J.-P. Zhou, Y.-O. Zhou, B.-H. Hao, T. Liu, Y. Yong, Int. J. Pharm. **389**, 1–2 (2010)

W. Martanto, J.S. Moore, O. Kashlan, R. Kamath, P.M. Wang, J.M. O'Neal, M.R. Prausnitz, Pharm. Res. **23**, 1 (2006)

M.G. McGrath, A. Vrdoljak, C. O'Mahony, J.C. Oliveira, A.C. Moore, A.M. Crean, Int. J. Pharm. **415**, 1–2 (2011)

D.C. Miller, B.L. Boyce, M.T. Dugger, T.E. Buchheit, K. Gall, Sensors Actuators A Phys. **138**, 1 (2007)

J. O'Brien, M. Bedoni, A. Blake, J. Scully, E. Forvi, M. Casella, F. Gramatica, C. O'Mahony. Proc. Micromechanics Europe, Toulouse, France, 20–22 September (2009).

C. O'Mahony, F. Pini, K.G. McCarthy, Sensors Actuators A Phys. **186**, 130 (2012)

S.-J. Paik, S. Byun, J.-M. Lim, Y. Park, A. Lee, S. Chung, J. Chang, K. Chun, D. Choa, Sensors Actuators A Phys. **114**, 276 (2004)

J.H. Park, M.G. Allen, M.R. Prausnitz, J. Control. Release **104**, 1 (2005)

M. Pearton, C. Allender, K. Brain, A. Anstey, C. Gateley, N. Wilke, A. Morrissey, J.C. Birchall, Pharm. Res. **25**, 2 (2008)

R. Pettis, A.J. Harvey, Ther. Deliv. **3**, 3 (2012)

F. Pini, C. O'Mahony, K.G. McCarthy. Proc. IEEE Int. Conf. Microelectronic Test Structures (ICMTS), (2012).

N. Roxhed, T.C. Gasser, P. Griss, G.A. Holzapfel, G. Stemme, J. Microelectromech. Syst. **16**, 6 (2007)

T.R. Singh, N.J. Dunne, E. Cunningham, R.F. Donnelly, Recent Pat Drug Deliv. Formul. **5**, 1 (2011)

W.G. Smith, Comput. Struct. **28**, 5 (1988)

S.P. Sullivan, D.G. Koutsonanos, M. del Pilar Martin, J.-W. Lee, V. Zarnitsyn, N. Murthy, R.W. Compans, I. Skountzou, M.R. Prausnitz, Nat. Med. **16**, 8 (2010)

T. Tanner, R. Marks, Skin Res. Technol. **14**, 3 (2008)

D.J. Tobin, Chem. Soc. Rev. **35**, 1 (2006)

K. van der Maaden, W. Jiskoot, J. Bouwstra, J. Control. Release **161**, 2 (2012)

A. Vrdoljak, M.G. McGrath, J.B. Carey, S.J. Draper, A.V.S. Hill, C. O'Mahony, A.M. Crean, A.C. Moore, J. Control. Release **159**, 1 (2012)

J.G. Webster, *Medical instrumentation: Application and design*, 4th edn. (Wiley, NJ, 2010)

N. Wilke, A. Morrissey, J. Micromech. Microeng. **17**, 2 (2007)

N. Wilke, A. Morrissey, C. Hibert, J. O'Brien, Sensors Actuators A Phys. **123–124**, 1 (2005a)

N. Wilke, A. Mulcahy, S.-R. Ye, A. Morrissey, Microelectron. J. **36**, 7 (2005b)

N. Wilke, M.L. Reed, A. Morrissey, J. Micromech. Microeng. **16**, 4 (2006)